Journal of
Synchrotron
Radiation

ISSN 0909-0495

Received 12 June 2007
Accepted 28 August 2007

In situ high-energy X-ray diffraction study of a bioactive calcium silicate foam immersed in simulated body fluid

V. FitzGerald,[a]* K. O. Drake,[b] J. R. Jones,[c] M. E. Smith,[b] V. Honkimäki,[d] T. Buslaps,[d] M. Kretzschmer[d] and R. J. Newport[a]

[a]School of Physical Sciences, University of Kent at Canterbury, Canterbury CT2 7NH, UK, [b]Department of Physics, University of Warwick, Coventry CV4 7AL, UK, [c]Department of Materials, Imperial College London, London SW7 2AZ, UK, and [d]Materials Science Group, European Synchrotron Radiation Facility, BP 220, F-38043 Grenoble CEDEX, France.
E-mail: vf22@kent.ac.uk

The method of *in situ* time-resolved high-energy X-ray diffraction, using the intrinsically highly collimated X-ray beam generated by the European Synchrotron Radiation Facility, is demonstrated. A specially designed cell, which allows the addition of liquid components, has been used to study the reaction mechanisms of a foamed bioactive calcia–silica sol–gel glass immersed in simulated body fluid. Analysis of the X-ray diffraction data from this experiment provides atomic distances, *via* the pair correlation functions, at different stages of the dissolution of the glass and of the associated calcium phosphate, and ultimately hydroxyapatite, *i.e.* bone mineral, formation. Hence, changes in the atomic scale structure can be analysed as a function of reaction time, giving an insight into the evolution of the structure of both the glass matrix and the hydroxyapatite surface growth.

Keywords: high-energy X-ray diffraction; glass structure; bioactive glass; *in situ* diffraction.

1. Introduction

1.1. Bioactive calcia–silica sol–gel foams

The sample of interest is a sol–gel-derived bioactive glass of the composition $(CaO)_{0.3}(SiO_2)_{0.7}$, designated S70C30 hereafter, which has been foamed in order to mimic the interconnected macroporous network of trabecular bone. Bioactive glasses bond to bone and stimulate bone cells at the genetic level. Bone bonding is due to the formation of a hydroxycarbonate apatite (HCA) layer on contact with body fluid, and cell stimulation is due to the release of Si and Ca ions. The foams have a hierarchical porous structure, with macropores in excess of 500 μm connected by pore windows with diameters in excess of 100 μm and a nanoporous texture (pore diameters 10–20 nm) (Jones *et al.*, 2006). The interconnected macroporous network provides the potential for cell migration, tissue in-growth and vascularization (Sepulveda *et al.*, 2002; Saravanapavan *et al.*, 2004; Pereira *et al.*, 2005). However, it is the nanoscale pores which contribute most heavily to the surface area, which determines the rate of dissolution and the rate of calcium phosphate deposition and growth. The foam scaffolds have been found to stimulate human bone cells to form mineralized bone nodules within 14 days of culture without the addition of supplementary growth factors (Jones *et al.*, 2007). The pore morphology affects cell attachment as well as bone mineral formation. The materials processing stages are shown in Fig. 1.

A full description of the preparation method can be found by Sepulveda *et al.* (2002). The samples comprise foams sintered to 873, 1073 and 1273 K.

1.2. ESRF beamline

With the development of modern synchrotron sources, high-energy X-ray diffraction is starting to play an important role in the characterization of bulk functional materials. The high-energy scattering beamline ID15 at the European Synchrotron Radiation Facility (ESRF, Grenoble, France) offers a large flux of highly collimated photons in the energy range 30 keV up to 1000 keV. This radiation is available together with a versatile experimental set-up, and the beamline therefore has a high potential for studies across a wide spectrum of scientific research. Specifically, the reasons for using ID15 in the materials science context of the present work are as follows.

(i) The availability of high-energy X-rays enables diffraction data to be recorded over a large dynamic range (noting that this range is described using the modulus of the wavevector transfer, $Q = 4\pi \sin\theta/\lambda$) and hence provides good real-space resolution ($\Delta r \simeq 2\pi/Q_{max}$) which is important if one

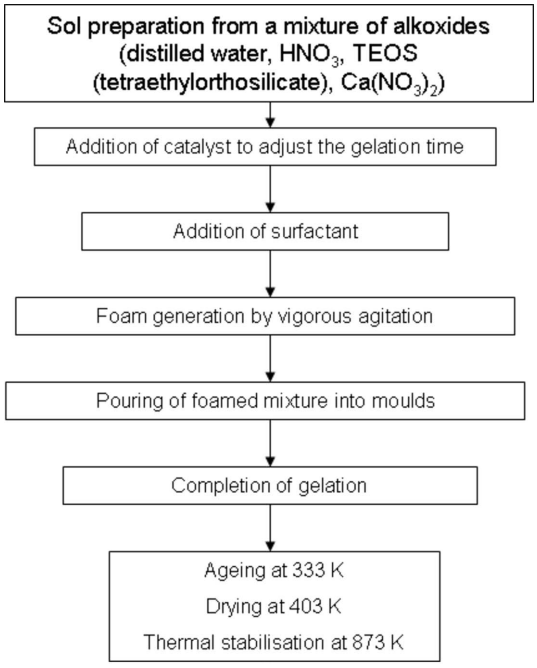

Figure 1
Flow chart of the sol–gel preparation process.

needs to resolve closely spaced pair correlations in an amorphous material.

(ii) The large X-ray flux, and the use of an on-line solid-state image-plate detector, makes it possible to acquire individual data sets over a very short period of time whilst retaining a satisfactory signal-to-noise ratio, so that good time resolution can be achieved.

1.3. Previous experiments

Recent work has highlighted the potential of sol–gel-derived calcium silicate glasses for the regeneration or replacement of damaged bone tissue. The mechanism of HCA layer formation and the requirements for optimization of the properties of these materials are as yet only partially understood, but have been linked in a previous study (Skipper *et al.*, 2005) to the particular nature of the calcium site in the glass, and to the way in which this controls the calcium dissolution from the glass matrix. This previous study was performed on powdered calcium silica sol–gel glasses of the composition $(CaO)_{0.3}(SiO_2)_{0.7}$, S70C30, which is the most highly bioactive composition of calcia–silica sol–gel glass (Skipper *et al.*, 2004). However, arguably the more interesting topical method for the production of bioactive glass scaffolds, with a similar morphology to trabecular bone, is the foaming of sol–gel-derived bioactive glasses (Jones *et al.*, 2006). Whilst it is not anticipated that there will be a significant difference between the foamed and powdered glasses in terms of the atomic scale structure (it is the nature of the porosity that differentiates the two forms of calcium silicate material), it is nevertheless important to investigate in more detail the nature of the reaction mechanisms involved. Thus, the analogous experiment to that of Skipper *et al.* (2005) has now been undertaken on these novel foamed bioactive calcia–silica sol–gel glasses, but using genuinely *in situ* and time-resolved methods.

In an earlier study (Skipper *et al.*, 2005) on the higher-density sol–gel-derived glasses, complex multi-stage dissolution and mineral growth phases were observed as a function of reaction time with simulated body fluid (SBF) of between 30 min and 7 d. The new methodology provides insight into the structure of key sites in these materials as they evolve through the various stages involved in the glass–SBF reaction. It thereby allows a detailed study of the mechanisms of reaction rather than merely providing a limited number of 'snapshots' at pre-defined times within a 'stop–go' experiment, in which the reaction was halted using an acetone wash and the resultant samples were then dried. Thus, the present study not only allows the careful study of the reaction, with significantly finer time steps, on a single sample, but moreover allows that study to take place with the sample fully immersed in SBF (*i.e.* 'wet'); it is therefore possible to comment more generically on their behaviour as bone regenerative materials.

The experiments described herein were focused on examining foamed calcium silicate sol–gel samples in order to investigate (i) the effects on initial structure and HCA layer formation of foamed compared with non-foamed samples, and (ii) the effects on the underlying structure of calcining foam preforms in the range 873–1273 K.

Extensive measurements of bioactivity in previous studies (Sepulveda *et al.*, 2002; Saravanapavan *et al.*, 2003; Skipper *et al.*, 2005) have shown that the above factors have profound effects on the bioactivity of non-foamed calcium silicates. The aim of this diffraction experiment is therefore to relate this prior knowledge to the underlying structure of the calcium silicate network within a genuinely *in situ*/time-resolved environment, and understand any difference in the effects these factors have on the kinetics and structure of *in vitro* HCA formation in the case of a foamed sample.

2. Experimental method

2.1. Experiment set-up

SBF treatments were carried out *in situ* whilst high-energy X-ray diffraction (HEXRD) data were collected on beamline ID15B at the ESRF. Samples of foam were held in a specially made cell, which could be rotated, and heated in the beam (the temperature was kept at 310 K, *i.e.* to mimic the *in vivo* environment, throughout the reaction by illumination using a halogen lamp, and monitored using a thermocouple). The cell is designed such that it allows *in situ* mixing of the sol–gel precursors (*i.e.* for a study of the sol–gel processing itself, see Drake, 2006) or for the addition of liquid components, as was necessary for the present case. A diagram of the *in situ* cell is shown in Fig. 2(*a*). The cell was built to hold a sample of foam in the beam whilst SBF is passed over it by rotating the entire cell throughout the reaction. As shown in Fig. 2(*b*), a cuboid sample of foam was held in place by two aluminium prongs. In order to retain the SBF in the cell, thin polymide (Kapton) windows were used, held against an 'O'-ring seal. The sample

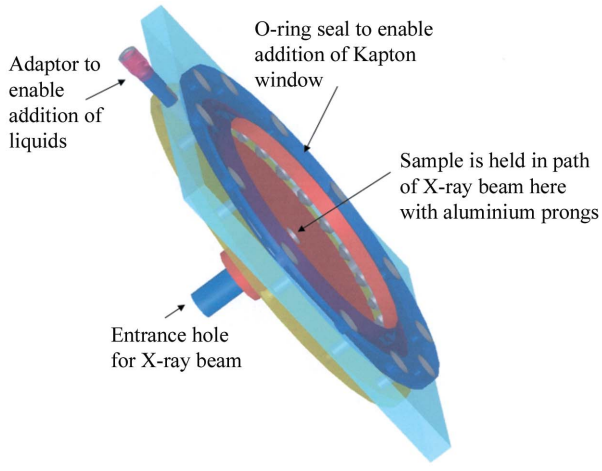

(*a*)

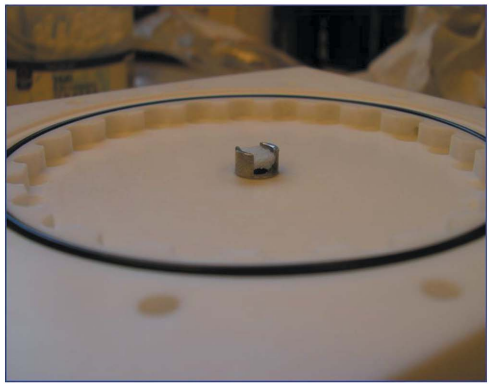

(*b*)

Figure 2
(*a*) Schematic diagram of the *in situ* cell. (*b*) Photograph showing how the sample was loaded into the *in situ* cell.

cell was positioned in the 0.25 mm^2 X-ray beam, ensuring that the beam travelled through the middle of the cell and had no contact with the aluminium prongs.

The X-ray photon energy was set to 97.5 keV, corresponding to a wavelength of $\lambda = 0.127$ Å. The beam size was collimated to 0.5 mm $\times$ 0.5 mm. The cell was positioned so that the sample-to-detector distance was 300 mm, which enabled a Q range of $\sim$2 to 23 Å^{-1} to be detected by the MAR 345 area detector. The experimental set-up is shown in Fig. 3.

2.2. Experimental technique

A diffraction pattern was collected with SBF only in the cell in order to provide a suitable background. The dimensions of the sample and its mass were measured before and after each reaction. After taking several scans of the unreacted sample with Kapton windows in place, the SBF was injected into the cell; the cell was then set rotating, and data collection was begun within approximately 5 min. Complete diffraction patterns were taken on a rolling basis every $\sim$50 s for the first 20 min, after which a pair of comparable $\sim$50 s scans were taken every 15 min. The reaction was monitored for up to 16 h. When the reaction was stopped, the sample was removed

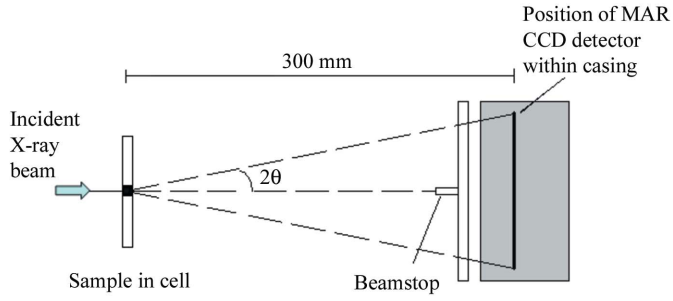

Figure 3
Schematic diagram of the experimental set-up.

and dried and its mass and dimensions post-reaction were measured.

3. Data reduction and analysis

3.1. Normalization and background removal

The two-dimensional images collected by the MAR 345 detector were radially integrated about the centre of the image. The centre of the image and also the tilt of the detector were found and corrected for using software written, in-house at the ESRF, in *Matlab* code.

Data analysis requires that the density and the composition of the sample is known; this creates obvious difficulties in the case of a time-resolved study of an *in situ* reaction. We have made an *ad hoc* assumption that the mass changes linearly with time, which therefore gave a corresponding density for the sample in the beam for each scan. Also, previous results (reproduced in Fig. 4) show the change of composition of a broadly similar sample with time immersed in SBF, measured *ex situ*; these were used to estimate the composition of the sample in the beam for each scan.

Each radial integration was normalized to the incident beam intensity. Corrections are made for the absorption due to the sample as well as for the absorption due to the air along the X-ray's optical path. The background associated with the

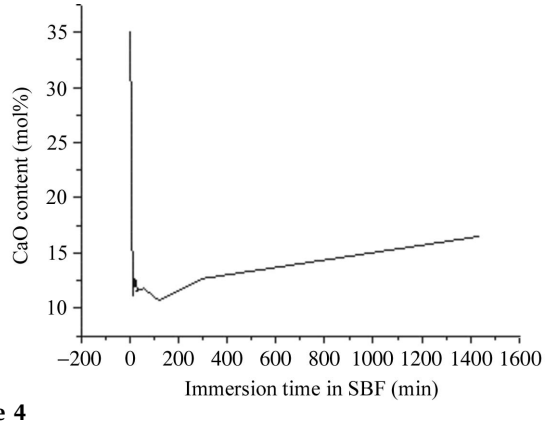

Figure 4
X-ray fluorescence data showing the calcium content of the glass as a function of time immersed in simulated body fluid; note the very rapid rate of loss during the first minutes of the reaction. (The variation of the phosphorus content of the glass is, approximately, the inverse of this, *i.e.* a rapid initial rise followed by a slower and more monatonic increase thereafter.)

scattering caused by the X-rays travelling through the air and empty cell is also measured and subtracted. Owing to self-shielding and excluded volume effects, the scattered intensity recorded with the SBF alone is actually greater than that recorded with a sample inserted; thus, a linearly scaled version of the measured SBF background must be removed such that the resultant was positive at all points. After 2.5 h in SBF at 310 K, there were no significant differences between any two scans taken in each 15 min period, so these scans were summed together, after being normalized, in order to improve the statistical quality.

3.2. Analysis

The next stage of analysis of X-ray diffraction data from an amorphous material involves the correction for absorption and inelastic scattering, and subtraction of the self-scattering term from the scattered intensity using a suite of programs written in-house, but based upon the methodology of Warren (1990) (see also Cole *et al.*, 2001). No correction was made to account for multiple scattering since this may be shown to be negligible in HEXRD in cases such as this where there is low total sample attenuation. The resultant structure factor, $S(Q)$, can reveal real-space structural information by Fourier transformation to obtain the pair distribution function, which is a measure of the radial distribution of neighbouring atoms around an atom taken to be at the origin,

$$T(r) = T_0(r) + \int_0^\infty QS(Q)M(Q)\sin(Qr)\,\mathrm{d}(Q), \qquad (1)$$

where $T_0(r) = 2\pi^2 r\rho_0$ (r is the atomic separation between atoms and ρ_0 is the macroscopic number density) and $M(Q)$ is a window function necessitated by the finite maximum experimentally attainable value of Q [in the present case, a Hanning function was adopted (Blackman & Tukey, 1959)].

Structural information can be obtained from the diffraction data by simulating the Q-space data and converting the results to r-space by Fourier transformation to allow comparison with the experimentally determined distribution function, and then iterating the process (Gaskell, 1991). The Q-space simulation is generated using the following equation,

$$p(Q)_{ij} = \frac{N_{ij}w_{ij}}{c_j}\frac{\sin QR_{ij}}{QR_{ij}}\exp\left(\frac{-Q^2\sigma_{ij}^2}{2}\right), \qquad (2)$$

where $p(Q)_{ij}$ is the pair function in reciprocal space, N_{ij}, R_{ij} and σ_{ij} are the coordination number, atomic separation and disorder parameter, respectively, of atom i with respect to j; c_j is the concentration of atom j, and w_{ij} is the associated weighting factor. The weighting factors are given by

$$w_{ij} = \frac{2c_ic_jf(Q)_if(Q)_j}{\overline{f(Q)}^2} \qquad \text{if } i \neq j, \qquad (3)$$

or

$$w_{ij} = \frac{c_i^2 f(Q)_i^2}{\overline{f(Q)}^2} \qquad \text{if } i = j, \qquad (4)$$

where $f(Q)$ represents the Q-dependent X-ray form factors.

The data presented herein have only been analysed semi-quantitatively owing to the limitations of this study. During the *in situ* experiment, the composition and density of the sample at each stage had to be estimated as there was no way of measuring these quantities during the reaction. X-ray fluorescence data from previous work on unfoamed S70C30 were used to estimate the composition of the sample at each stage, and the density was assumed to change linearly with time, and the mass of the sample before and after the reaction was used to calculate it. Therefore, the data in question are now analysed semi-quantitatively, as the areas of the peaks are subject to uncertainty on an absolute scale, although relative trends will be reasonably reliable, and in the context of attempting to follow the reaction processes these are extremely useful despite the limitations. Peak positions in the data should be reliable, and can provide some structural information on the sample during the reaction.

4. Results and discussion

Fig. 5 shows the diffraction data for the unreacted foam samples, calcined at 873, 1073 and 1273 K; there are evident differences between each sample. The main difference between the foam heated to 873 K and the foam heated to 1073 K in the $S(Q)$ functions is the peak at 4.4 Å^{-1} which is more prominent in the 1073 K foam $S(Q)$ than in the 873 K foam $S(Q)$, where it appears only as a shoulder. The Q-space data for the 1273 K foam shows that this sample is at least partially crystalline, as evidenced by the many Bragg peaks, whereas the other two samples appear to be amorphous. This agrees with conventional X-ray diffraction spectra obtained on S70C30 foams, which were shown to be amorphous after sintering for 2 h at 1073 K and showed Bragg peaks corresponding to natural wollastonite after sintering for 2 h at 1273 K (Jones *et al.*, 2006). The Bragg peaks revealed in the present data are indicative of a mixture of wollasonite and pseudo-wollastonite type material (Fletcher *et al.*, 1996; Ohashi, 1984; Yang & Prewitt, 1999).

When looking at the corresponding real-space data associated with these three samples, three major features are seen to occur in all $T(r)$ functions. The first major peak is assigned to the Si—O correlation at 1.61 Å. The second peak, centred at 2.5 Å, is associated with the Ca—O first-shell correlations and the second-shell O···O correlations. The third peak, centred at 3.2 Å, is associated with the Si···Si correlation and the Si···Ca correlation shells. To assign these peaks in the present samples, data from a previous experiment on the same composition of (non-foamed) glass were used (Skipper *et al.*, 2005).

Fig. 6 shows the three $T(r)$ functions together. The differences between the 873 K and 1073 K foams are small, and mostly visible in the peak centred at 2.5 Å. Our modelling shows that this broad peak comprises three Ca—O correlation shells at 2.3, 2.5 and 2.8 Å, along with the O···O coordination at 2.6 Å. The 1073 K foam appears to have a more prominent peak at 2.3 Å and a weaker peak at 2.8 Å than the 873 K foam. This is taken to imply that there is a difference in calcium

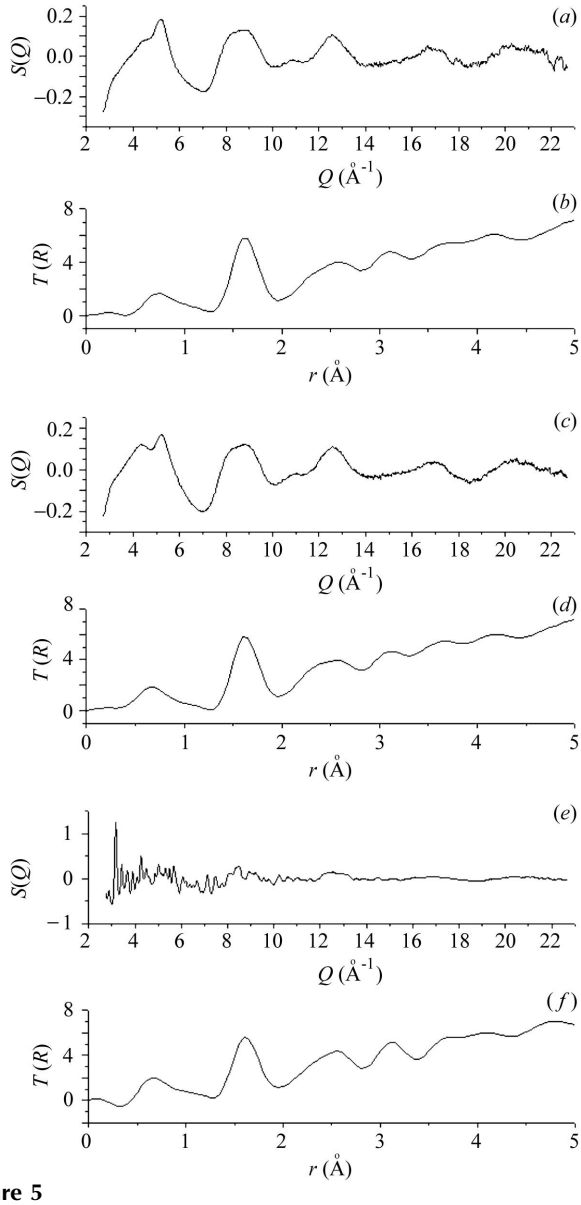

Figure 5
High-energy X-ray diffraction data for the unreacted foam: (*a*, *c*, *e*) *Q*-space structure factor, $S(Q)$, and (*b*, *d*, *f*) pair distribution function, $T(r)$, at 873 K, 1073 K and 1273 K, respectively.

environment between the two samples. The 1273 K foam appears to have a stronger contribution from Ca—O peaks at 2.3 and 2.5 Å, and a weaker contribution from the Ca—O peak at 2.8 Å than either of the other two samples. Jones *et al.* (2006) showed the 1273 and 1073 K foams to form HCA layers at three days in SBF compared with 8 h for the 873 K foam. This result could indicate that the Ca—O correlation at 2.8 Å is the correlation relating to the dissolution of Ca in the first stage of reaction in SBF. Given that the 1273 K foam shows strong Bragg peaks in the *Q*-space data, with a strong peak at 2.53 Å and a slight shoulder at 2.3 Å in the corresponding *r*-space data, we may surmise that at the near-neighbour scale this sample has structural similarities to a pseudo-wollastonite type of material in which the Ca environment is eight-fold coordinated with an average Ca—O correlation occurring at

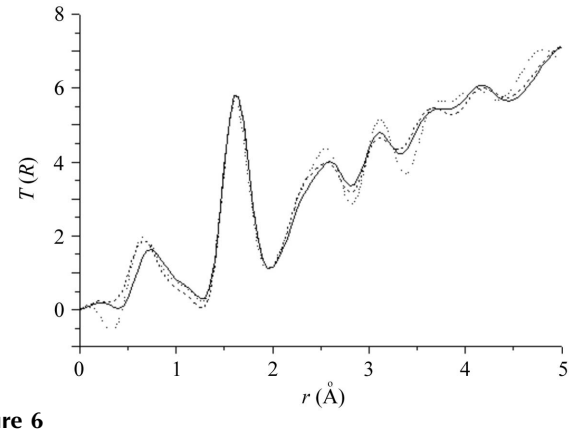

Figure 6
High-energy X-ray diffraction data for the unreacted foam pair distribution functions, $T(r)$, corresponding to 873 K (black line), 1073 K (dashed line) and 1273 K (dotted line).

~2.53 Å (Fletcher *et al.*, 1996; Yang & Prewitt, 1999; Sowrey *et al.*, 2004). We note, however, that pseudo-wollastonite has a particularly diffuse Ca—O environment in which bond lengths range from 2.28 to 2.72 Å.

Figs. 7 and 8 show the *in situ* diffraction data for the 873 K and 1073 K foams, respectively. This is to compare a highly bioactive foam with a less bioactive foam; no *in situ* data were taken for the foam sintered to 1273 K.

Fig. 7 shows the *in situ* diffraction data for the foam sintered at 873 K. The reaction was followed for ~16 h. The data show that, within a few minutes of the SBF being added to the glass, changes in $S(Q)$ are apparent. After ~1 h there is clear evidence for the formation of Bragg diffraction peaks, which indicates the growth of crystallites in the sample. After ~3 h the Bragg peaks appear very strong, indicating a significant polycrystalline layer. The peaks are indicative of tricalcium phosphate and hydroxyapatite (HA), and, after 5 h, peaks indicative of HCA are visible, *e.g.* the peak at 5.08 Å^{-1} (Fletcher *et al.*, 1996). The peaks are atop the underlying amorphous pattern. While a comparable qualitative observation was made in the context of the *ex situ* unfoamed samples (Skipper *et al.*, 2005), in the case of the foamed samples examined in this paper the polycrystalline phase remains present in the glass right up until the reaction was stopped at ~16 h, whereas in the unfoamed materials the initial crystallite growth was seen to become more like an amorphous HA at 10 h of immersion. Thus, it is apparent that the porosity and/or calcination temperature-linked glass network connectivity of the material has an important effect on its *in vitro* reaction with SBF.

The first peak in the $T(r)$ functions is assigned to the Si—O peak in the unreacted data, but to a combination of Si—O and P—O correlations in the reacted-glass data. The peak is at ~1.6 Å for all data runs, and the change in height of the peak may be associated with the fluctuating phosphorus content in the sample as the reaction takes place. A previous study (Skipper *et al.*, 2005) showed that the phosphorus content mirrors that of calcium and increases sharply when the reaction begins, before undergoing a series of oscillations during

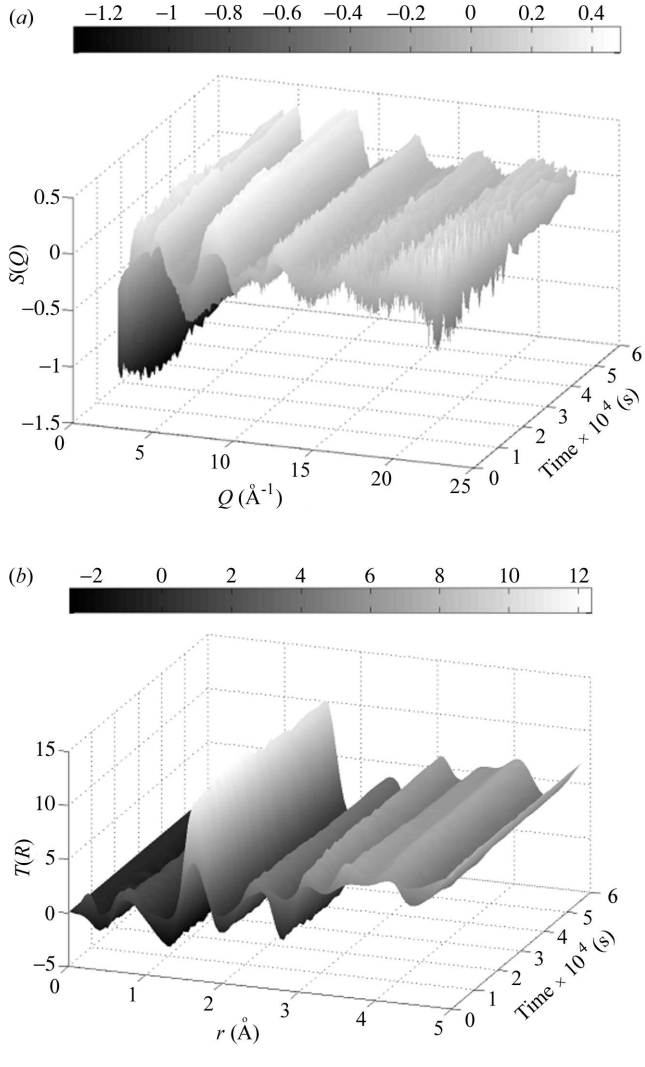

Figure 7
High-energy X-ray diffraction data for the 873 K foam throughout reaction in simulated body fluid for ∼16 h. (*a*) *Q*-space structure factors, *S*(*Q*), and (*b*) pair distribution functions, *T*(*r*).

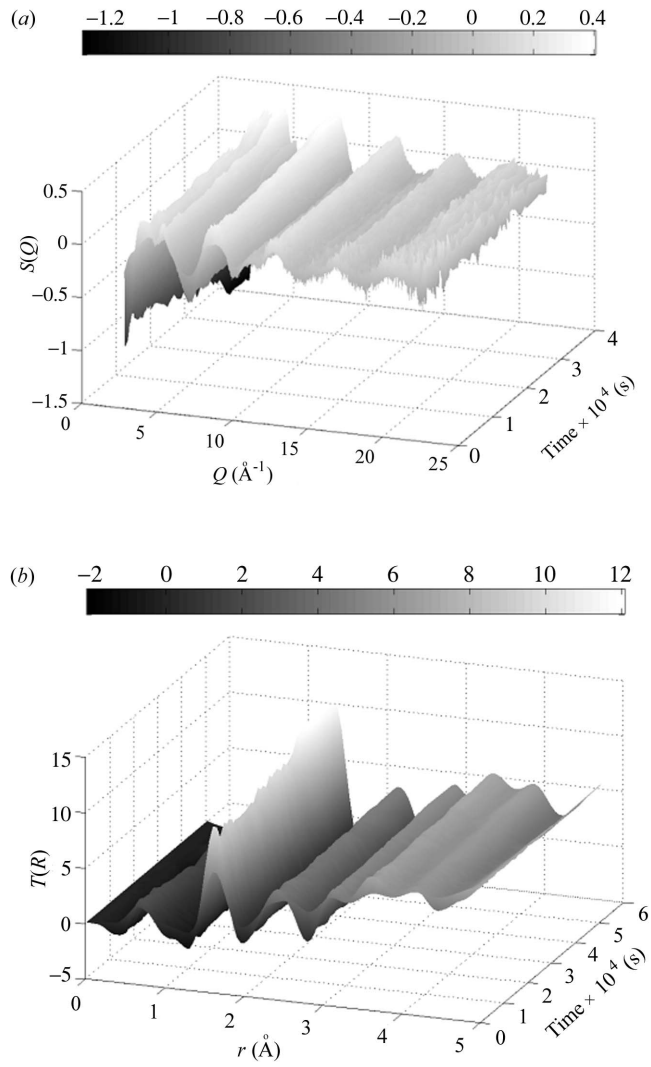

Figure 8
High-energy X-ray diffraction data for the 1073 K foam throughout reaction in simulated body fluid for ∼16 h. (*a*) *Q*-space structure factors, *S*(*Q*), and (*b*) pair distribution functions, *T*(*r*).

the initial reaction period and then levelling off. The first peak in the *T*(*r*) functions shows an increase in intensity as soon as the reaction is started, which then increases slowly during the reaction, fluctuating slightly. This peak intensity change is in unison with the measured phosphorus content for the first 16 h of reaction, as seen in the work of Skipper *et al.* (2005).

The second feature in the *T*(*r*) functions centred at 2.5 Å, arising from both Ca—O and O···O correlations, appears as a broad peak in the unreacted sample, and then becomes a narrower feature centred at 2.4 Å as the reaction proceeds. The data imply that, from near the point at which the reaction is started, there is a rapid impact on the Ca—O distances of 2.3 and 2.8 Å, which is almost certainly associated with initial calcium loss, as previously observed (Newport *et al.*, 2007).

In molecular dynamics simulations of a sol–gel glass of the same composition and density as that studied by Skipper *et al.* (2005), three Ca—O environments were also postulated (Mead & Mountjoy, 2006). The three environments were shown to correspond to Ca—O_{nb} (∼2.3 Å), Ca—OH (∼2.5 Å) and Ca—O_b (∼2.7 Å). The studies performed by Skipper *et al.* (2005) and Newport *et al.* (2007) indicated that during the initial 30 min of reaction time the peak at 2.3 Å decreased significantly in area, and the peak at 2.5 Å became dominated by the peak at 2.7 Å. This is indicative of the formation of calcium phosphates after immersion in SBF as the Ca—O correlations in calcium phosphates are found at longer bond distances. In the *in situ* data presented herein, the peak at 2.3 Å significantly decreases in area with the introduction of SBF; however, the peak at 2.5 Å increases with intensity, and the peak at ∼2.7 Å disappears. This could also be indicative of the growth of calcium phosphates, given the large number of possible alternatives. However, it certainly indicates that during the *in situ* experiment we observe more Ca—OH correlations, which may not have been apparent in the *ex situ* 'stop–go' reaction data owing to the drying of the samples after reaction in SBF.

There are other significant differences in the present *in situ* data compared with the previously observed *ex situ* data. It

appears from Fig. 7 that the O···O correlation peak, associated primarily with the host silica network, weakens as the reaction takes place, which indicates that the reaction is disrupting the underlying glass network. The O···O correlation is evidently moving to shorter distances, as the calcium is removed from the glass network and the growth of a calcium phosphate layer occurs. In addition, Fig. 7 also shows that the peak at ∼3.2 Å, associated with the Si···Si second-nearest-neighbour distance and the Si···Ca correlation, narrows and shifts slightly to higher *r*. As it is unlikely that the Si···Si bond distance is changing, this implies an increase in Si···Ca hetero-coordination and a decrease in Si···Si homo-coordination. This may be due to the growth of a calcium phosphate layer, followed by an increasingly ordered form of HA, and then HCA.

Fig. 8 shows the *in situ* diffraction data for the reaction of the 1073 K foam in SBF. Both the *Q*-space and the *r*-space data show that the reaction of the foam calcined to 1073 K is different in many ways from the 873 K calcined foam's reaction. Firstly, the *Q*-space data reveal that the Bragg peaks, which are beginning to form after only 1 h in SBF for the 873 K foam, start to form only much later on in the reaction for the 1073 K foam, at ∼8 h. The Bragg peaks associated with tricalcium phosphate and HA are visible, but in this case there is no indication of the growth of HCA. In the $T(r)$ functions, similar changes are occurring in the Si—O/P—O peak at 1.6 Å and in the peak corresponding to the Ca—O correlations and O···O correlations; however, they appear to be changing at a slower rate than for the 873 K foam. The main difference between samples, however, is observed in the peak at ∼3.6 Å, which in the 1073 K foam is present throughout the reaction, although becoming slightly narrowed and more prominent. In the 873 K foam, however, the corresponding peak at first becomes narrow and more prominent, but then ceases to change in height or width, after which the peak at 4.1 Å then becomes more prominent. At no point in the ∼16 h of the reaction for the 1073 K foam does the peak at 4.1 Å become more prominent than the peak at 3.6 Å. The peak at 3.6 Å was associated in the unreacted sample with Ca···Ca correlations, and with Ca···Ca and Ca···P correlations once the reaction has started. The peak at 4.1 Å may be associated with inter-tetrahedral P···P and P···O correlations in HA (or, were it present, HCA).

The techniques developed here have allowed the non-invasive *in situ* monitoring of the surface reactions of bioactive glass foams in real time. The results show that foams sintered at 873 K show indications of Bragg peaks after only 1 h of immersion, and after 5 h show Bragg peaks related to HCA. Foams sintered at 1073 K show the same reaction stages as the 873 K foam; however, the reaction appears to be occurring at a slower rate. Bragg peaks begin to form after 8 h of immersion, and they are indicative of tricalcium phosphate and HA but not HCA. The changes in dissolution and bioactivity are due to changes in the atomic structure which were shown in previous X-ray diffraction data brought about by sintering (Jones *et al.*, 2006). The changes in atomic structure dictate the nanopore size and specific surface area (SA/V). The modal nanopore size of foams sintered at 873 K was 17 nm (SA/V = 107 $m^2 g^{-1}$), while foams sintered at 1073 K had a modal nanopore size of 12 nm (SA/V = 42 $m^2 g^{-1}$).

5. Concluding remarks

We describe herein a method which may be used for *in situ* time-resolved high-energy X-ray diffraction studies of reaction mechanisms such as those involved when a bioactive calcia–silica sol–gel glass is immersed in simulated body fluid. Although, in this particular case, the method can only generate semi-quantitative data, it is nevertheless demonstrated that structural changes in the glass as a function of reaction time can be observed. Analysis of the X-ray diffraction data from this experiment yields reliable atomic distances (*i.e.* pair correlations) at different stages of the glass dissolution and of the surface-related calcium phosphate/hydroxyapatite formation. Changes in the atomic distances and relative coordination numbers may therefore be assessed as a function of time in relation to the structure of both the glass matrix and the reaction products, and thus allow an insight beyond the 'snapshots' available hitherto. This detailed structural information facilitates a clearer discernment of the ways in which materials processing affect a given sample; in the present case, to inform the optimization of calcium silicate materials used in tissue engineering applications.

Gabriela Gonzalez-Aviles is thanked for help with the experimental set-up on ID15. VF thanks the EPSRC and the University of Kent for her studentship. We wish to acknowledge the use of the EPSRC's Chemical Database Service at Daresbury. KOD thanks EPSRC and ESRF for a studentship. EPSRC are thanked for their support of the Kent–Imperial–Warwick collaboration on bioactive silicate-based materials.

References

Blackman, R. B. & Tukey, J. W. (1959). *The Measurement of Power Spectra From the Point of View of Communications Engineering.* New York: Dover.
Cole, J. M., van Eck, E. R. H., Mountjoy, G., Anderson, R., Brennan, T., Bushnell-Wye, G., Newport, R. J. & Saunders, G. A. (2001). *J. Phys. Condens. Matter*, **13**, 4105.
Drake, K. O. (2006). PhD thesis, University of Warwick, UK.
Fletcher, D. A., McMeeking, R. F. & Parkin, D. (1996). *J. Chem. Inf. Comput. Sci.* **36**, 746–749.
Gaskell, P. H. (1991). *Materials Science and Technology*, Vol. 9, edited by J. Zrzycky, p 175. Weinhaim: VCH.
Jones, J. R., Ehrenfried, L. M. & Hench, L. L. (2006). *Biomaterials*, **27**, 964–973.
Jones, J. R., Tsigkou, O., Coates, E. E., Stevens, M. M., Polak, J. M. & Hench, L. L. (2007). *Biomaterials*, **28**, 1653–1663.
Mead, R. M. & Mountjoy, G. (2006). *Chem. Mater.* **18**, 3956–3964.
Newport, R. J., Skipper, L. J., FitzGerald, V., Pickup, D. M., Smith, M. E. & Jones, J. R. (2007). *J. Non-Cryst. Solids*, **353**, 1854–1859.
Ohashi, Y. (1984). *Phys. Chem. Miner.* **10**, 217–229.
Pereira, M. M., Jones, J. R. & Hench, L. L. (2005). *Adv. Appl. Ceram.* **104**, 35–42.
Saravanapavan, P. & Hench, L. L. (2003). *J. Non-Cryst. Solids*, **318**, 1–13.

Saravanapavan, P., Jones, J. R., Pryce, R. S. & Hench, L. L. (2003). *J. Biomed. Mater. Res.* A**66**, 110–119.
Saravanapavan, P., Jones, J. R., Verrier, S., Shirtliff, V. J. & Hench, L. L. (2004). *J. Biomed. Mater. Eng.* **14**, 467–486.
Sepulveda, P., Jones, J. R. & Hench, L. L. (2002). *J. Biomed. Mater. Res.* **59**, 340–348.
Skipper, L. J., Sowrey, F. E., Pickup, D. M., Drake, K. O., Smith, M. E., Saravanapavan, P., Hench, L. L. & Newport, R. J. (2005). *J. Mater. Chem.* **15**, 2369–2374.
Skipper, L. J., Sowrey, F. E., Pickup, D. M., FitzGerald, V., Rashid, R., Drake, K. O., Lin, Z., Saravanapavan, P., Hench, L. L., Smith, M. E. & Newport, R. J. (2004). *J. Biomed. Mater. Res.* A**70**, 354–360.
Sowrey, F. E., Skipper, L. J., Pickup, D. M., Drake, K. O., Lin, Z., Smith, M. E. & Newport, R. J. (2004). *Phys. Chem. Chem. Phys.* **6**, 188–192.
Warren, B. E. (1990). *X-ray Diffraction.* New York: Dover.
Yang, H.-X. & Prewitt, C. T. (1999). *Am. Mineral.* **84**, 929–932.